Comparison of acoustic and hydrodynamic cavitation: material point of view

Julien Hofmann, Charles Thiébaut, Michel Riondet, Pierre Lhuissier, Sylvain Gaudion, Marc Fivel

Comparison of acoustic and hydrodynamic cavitation: material point of view

Julien Hofmann,[1,2] Charles Thiébaut,[1] Michel Riondet,[2] Pierre Lhuissier,[1] Sylvain Gaudion,[3] and Marc Fivel[1]
[1)] *Univ. Grenoble Alpes, CNRS, Grenoble INP, SIMaP, F-38000 Grenoble, France*
[2)] *Univ. Grenoble Alpes, CNRS, Grenoble INP, LEGI, F-38000 Grenoble, France*
[3)] *Laboratory General Electric Advanced Technology, F-38000 Grenoble, France*

(*Electronic mail: julien.hofmann@grenoble-inp.fr)

(Dated: 20 December 2022)

This study investigated the difference of mechanical response of the martensitic stainless steel X3CrNiMo13-4/S41500/CA6NM QT780 between hydrodynamic and acoustic cavitation erosion. Acoustic cavitation erosion tests have been performed using a 20 kHz ultrasonic horn located at 500 μm in front of a specimen. This experimental setup, known-as indirect method, is inspired from the ASTM G32 standard. Hydrodynamic cavitation erosion tests were conducted with classic experimental conditions of PREVERO device: a cavitation number of 0.87 corresponding to a flow velocity of 90 $m.s^{-1}$ and an upstream pressure of 40 bars. Results show that acoustic cavitation erosion generates small pits at high temporal frequency on the material while hydrodynamic cavitation erosion produces larger pits at a lower frequency. In addition, for a given exposure time the percentage of surface covered by the pits is smaller for acoustic cavitation than for hydrodynamic cavitation. Three successive steps have been identified during the damage process: persistent slip bands (PSB) first appear on the surface, cracks initiate and propagate at the PSB locations and non-metallic interfaces and finally parts of matter are torn off. A careful time examination of the same small area of the exposed sample surface by scanning electron microscopy (SEM) reveals that acoustic cavitation is faster to initiate damage than hydrodynamic cavitation.

I. INTRODUCTION

Cavitation denotes the phenomenon in which vapor bubbles form in a liquid after a local pressure drop below the saturated vapor pressure[1]. This phase transformation is common in hydraulic machinery: fuel injectors, valves, pumps and water turbines for example. The collapse of cavitation bubbles close to a solid surface can lead to harmful effects such as vibration, noise and erosion[2].

Cavitation erosion is known as a significant cause of loss of efficiency of hydraulic machinery. Surface modification is attributed to microjet and shock waves occurring during the collapse of multiple cavitation bubbles when it happens close to a material surface[3]. The collapse is a local and violent phenomenon: stress on the surface can reach few gigapascals[1] at a strain rate as high as 10^6 s^{-1}. If the stress resulting from the shock waves or micro jet impacts outreaches the yield stress of the material, a pit is created. Accumulation of these local plastic deformations on the surface increases the work hardening along the exposure time to cavitation. This will cause the material cracking and inescapably lead to mass loss[2,4–7]. Cavitation erosion can be investigated in laboratories using different devices such as vibratory cavitation apparatus or hydrodynamic tunnels. Each device has its own characteristics in term of material solicitations including flow velocity, impact frequency and impact loads which allows to investigate a wide range of aggressiveness conditions. The objective of the present work is to compare the mechanical response of a low-carbon martensitic stainless steel, commonly used in hydroelectric turbines, exposed to cavitation erosion from hydrodynamic and acoustic devices. Hydrodynamic cavitation is generated using a tunnel in which the flow velocity can be set to adjust the cavitation number[8–10]. Acoustic erosion cavitation testing, standardized by the ASTM G32, is one of the most popular laboratory technique[11–13], generally used for convenience and availability of commercial solutions. In the present study, based on surface and microstructure analysis, we point out the similarities and differences in the material response when exposed to these two loading conditions: hydrodynamic and acoustic cavitation. These results are discussed from the material point of view.

TABLE I. Chemical composition of main chemical elements of stainless steel X3CrNiMo13-4 QT780. Material has been analysed using X-ray fluorescence ★ and inert gas fusion elemental analyser ■. Chemical compositions are given in wt.% if not indicated.

	Cr★	Ni★	Mo★	C■	Mn★	S■ [ppm]
X3CrNiMo13-4 QT780	12.61	3.75	0.54	0.035	0.58	92

II. MATERIALS AND METHODS

A. Materials

In this research, the low-carbon X3CrNiMo13-4 QT780 martensitic stainless steel provided by Ugitech was chosen as the tested material. It was austenitising at 1100 °C, quenched and then double tempered at 600 °C for 4 h. The resulting material is composed of a martensitic matrix α' with lamellar reversed austenite γ_{rev} and residual delta ferrite δ-Fe. It shows high corrosion resistance and high mechanical strength. This material is thus widely used for water turbine manufacturing. Its chemical composition identified by X-ray fluorescence spectrometry and inert gas fusion elemental analysis

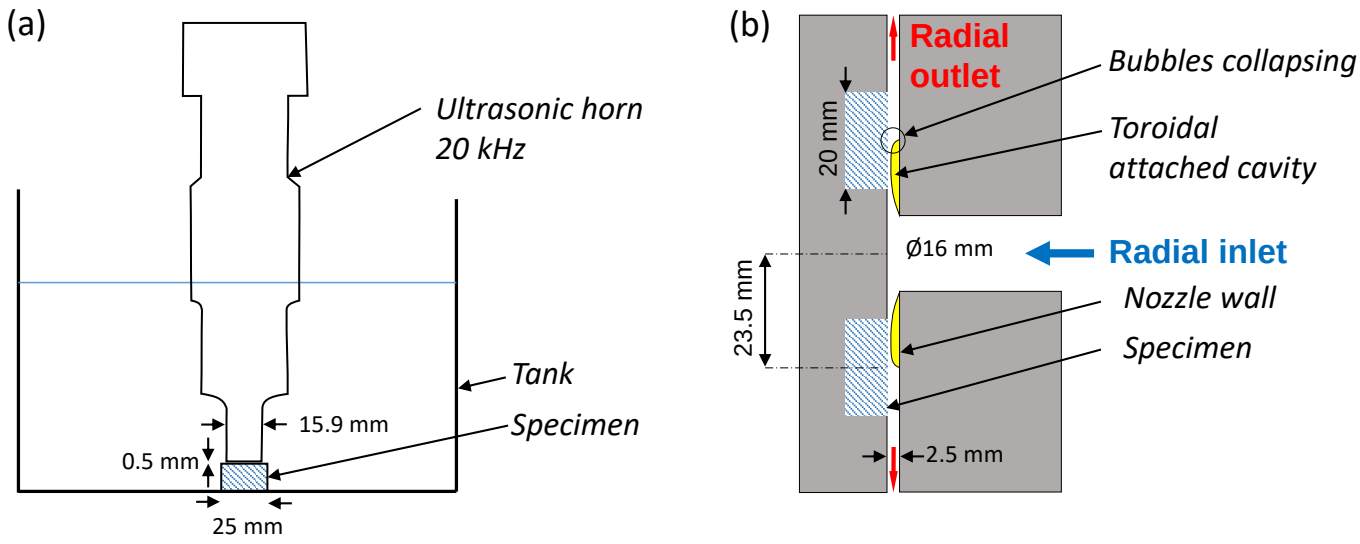

FIG. 1. Schematic of the devices used for the cavitation erosion experiments. (a) Acoustic cavitation apparatus: the specimen is located at 0.5 mm from the ultrasonic horn (indirect method). (b) Hydrodynamic tunnel: the samples are mounted in the zone of collapse of the cavitation cloud ; the cavitation number σ is here fixed at 0.870 corresponding to a flow velocity of 90 m.s^{-1} and upstream pressure of 40 bars.

(Leco CS744, USA) is given in TABLE I.

B. Cavitation erosion testing

Two in-house devices were used for generating two types of cavitation: acoustic and hydrodynamic. A 20 kHz ultrasonic transducer (Sinaptec Lab750, France) was used for the acoustic cavitation erosion tests using indirect method. As shown in FIG. 1(a) stationary specimen is placed at 0.5 mm below the ultrasonic horn vibrating at 20 kHz with a peak-to-peak amplitude of 50 μm. The distance between specimen and ultrasonic horn was measured using a x100 optical camera (Dino-Lite AM4815ZTL, Taiwan) and adjusted using a micrometric motorized stage (OWIS LTM120, Germany). The erosion tests were performed in water at 23 $\pm$ 2 °C containing 4.2 mg.L^{-1} of dissolved oxygen (Hanna Instruments HI98199, United States). Specimen consisted of cylinders with a height of 5 mm and diameter of 25 mm.

Hydrodynamic erosion tests were conducted using a 40 bars cavitation flow tunnel (PREVERO) located at LEGI laboratory[14]. The water flow is created using a centrifugal pump rotated by an 80 kW electric motor. Pressurization of the liquid is performed using nitrogen gas on the free surface of a water tank. Tap water temperature was kept constant at 23 $\pm$ 2 °C using a heat exchanger. As illustrated in FIG. 1(b) on a cross section view, a gap of 2.5mm is defined between the nozzle wall and the specimen so that the radial outlet flow reach a maximum velocity of 90 m.s^{-1} leading to the formation of cavitation sheets. The dynamics of cavitation in PREVERO tunnel has been studied by Gavaises et al.[15] using high-speed visualisation and large eddy simulations. Cavitation firstly forms at the turn of the nozzle due to the rapid acceleration of the liquid. The toroidal cavitation cloud then grows as it is transported by convection until it reaches a maximum distance from the nozzle exit. The closure of the cavity, which is a saddle point, is known for generating instability[16]. It hence creates a re-entrant liquid jet between the nozzle wall and the vapor cavity which separates the cavitation cloud from the wall. When the cavity is totally detached from the wall, a bubbles cloud is created. A significant vorticity forms due to opposite directions of liquid re-entrant jet and main flow, which makes bubbles cloud rotating and travelling downstream. When the centrifugal force, made by vorticity, is counterbalanced by the surrounding pressure, the edge of the bubble cloud starts to collapse. Specimen are inserted in the middle of the zone of cloud collapse. They consist of cylinders with a height of 6 mm and diameter of 20 mm. Hydrodynamic cavitation erosions tests were realized at a constant cavitation number σ = 0.870 $\pm$ 0.001. A complete description of this cavitation flow loop has been made by Franc et al.[14].

Surface specimen exposed to acoustic and hydrodynamic cavitation have been polished using identical procedure. Specimen have been mechanically grounded using SiC abrasive papers from P400 to P1200 followed by polishing step using diamond suspension 9 μm, 3 μm and 1 μm. Finally, vibratory polishing (VibroMet, Buehler, United States) has been carried out using a 0.06 μm colloidal silica solution. After polishing and after each cavitation erosion tests, specimen were carefully cleaned using ethanol and soap.

C. Characterisation

1. *Surface analysis*

Morphology of the eroded surfaces was observed after each cavitation erosion tests using an optical profilometer (Zegage Pro HR, Zygo, United States) and a scanning electron microscope (Gemini ultra 55 SEM, Zeiss, Germany). For observing

the same region for the different exposure time, the specimen has been marked using two Vickers indents with a force of 10 N (Presi MX7, France). For identifying the pits created by the collapse of cavitation bubble, a cut-off depth -0.2 μm has been applied below the original virgin material surface. The cut-off value has been chosen large enough to avoid the effect of the surface roughness and separate the pits and small enough for truthfully measure the pits' shape.

2. *Phase analysis*

X-ray diffraction (XRD) was employed to identify and quantify the phases existing in the studied material X3CrNiMo13-4 QT780. Analysis was realized using a Cu-K_α radiation (λ = 1.5406 Å) in 30-130° interval using a scanning speed of 0.2 °.min^{-1} with a step size of 0.02° (Malvern Panalytical, X'Pert Pro, England). The volume of fraction of reversed austenite γ_{rev} was estimated using the semi-quantitative method proposed by Tanaka and Choi[17] using the integrated intensities of main peak of reversed austenite (γ_{rev}) and martensite (α'). Equations 1 and 2 below were used to calculate the volume fraction of reversed austenite:

$$V_{\gamma_{rev}} + V_{\alpha'} = 1 \tag{1}$$

$$V_{\gamma_{rev}} = \frac{1.4 I_{\gamma_{rev}(111)}}{I_{\alpha'(110)} + 1.4 I_{\gamma_{rev}(111)}} \tag{2}$$

where $V_{\gamma_{rev}}$ is the γ_{rev}-phase volume fraction, $V_{\alpha'}$ is the α'-phase volume fraction, $I_{\gamma_{rev}(111)}$ is the integrated intensity of the γ_{rev}-phase (111) diffraction peak and $I_{\alpha'(110)}$ is the integrated intensity of the α'-phase (110) diffraction peak.
Microstructural investigation at submicrometer scale has been carried out using electron backscatter diffraction (EBSD). Experiment has been realized using a Zeiss Gemini SEM 500 FEG equipped with an EBSD detector (EDAX, Hikari Super, United States) with a step size of 100 nm. XRD and EBSD analysis were made on specimen prepared using the same methodology as described in II B.

III. RESULTS AND DISCUSSIONS

A. Pitting rate

At the very beginning of cavitation exposure, isolated pits appear on the material surface. It is hence possible to count the number of pits and measure their diameter. FIG. 2 presents the cumulative histograms of pitting rates versus pit equivalent diameter both for acoustic and hydrodynamic cavitation for an exposure time of 16 min. Cumulative pitting rate is defined as the number of pits per unit of time and per unit area counted with a equivalent diameter exceeding a given value. Pit can be more complex than circular shaped because of the appearance of re-entrant jet and the toroidal structure of the cavity which

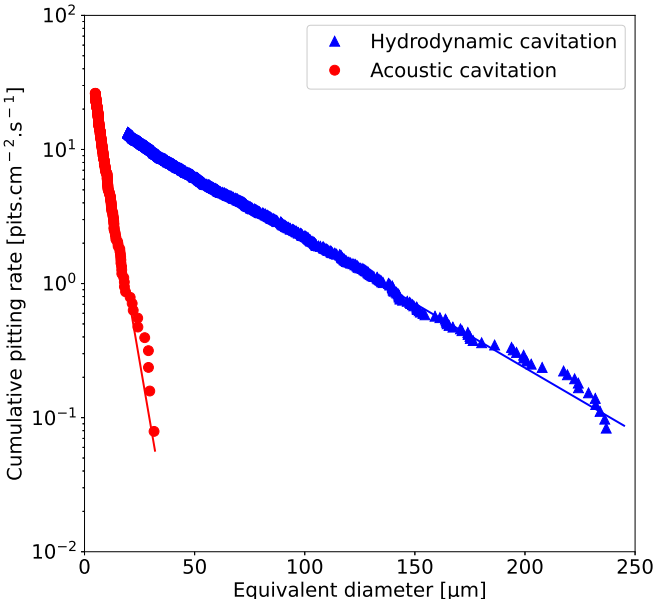

FIG. 2. Cumulative pitting rate as a function of pit diameter on X3CrNiMo13-4 QT780 stainless steel. Straight lines correspond to exponential distributions. Acoustic cavitation tests have been carried out using an ultrasonic horn at 20 kHz on a sample located at 500 μm during 16 min. Hydrodynamic cavitation test has been carried out in the LEGI cavitation erosion facility at a upstream pressure of 40 bars and at a constant cavitation number of 0.870 during 16min. Pits have been counted and measured using a 0.2 μm cut-off.

could create smaller bubbles which may collapse as well[10,18]. As shown in FIG. 2, histograms are well fitted by straight lines in semi-logarithmic scales: the cumulative pitting rate can be approximated by an exponential decay law for pits from a few micrometers up to 250 μm. The slope of the straight lines is -9.59 10^{-3} pits.cm^{-2}.s^{-1}.μm^{-1} for hydrodynamic cavitation and -9.56 10^{-2} pits.cm^{-2}.s^{-1}.μm^{-1} for acoustic cavitation i.e. one order of magnitude higher.

FIG.2 shows that the bigger the pit size, the smaller the pitting rate which expresses that vapor cavities produce few large pits and an important number of small pits whatever the type of cavitation.

Hydrodynamic cavitation erosion makes large pits at a small pitting rate and, conversely, acoustic cavitation erosion creates small pits at a high pitting rate. The difference of pit sizes could be attributed to the difference of the shape of the vapor cavity clouds: using ultrasonic horn, acoustic cavitation is known for generating small bubbles with a diameter between few microns up to hundreds of microns[19,20]. On the other hand, hydrodynamic cavitation cloud is made of bubbles with a wide dispersion of sizes and pressures as estimated by Roy[21].

Moreover for hydrodynamic cavitation, the shedding frequency, i.e. the collapse frequency, has been approximately evaluated by Gavaises et al.[15] and Ylonën et al.[22] to 1,600 Hz for a downstream pressure of 19 bar and a cavitation number equal to 0.87 corresponding to the experimental conditions of our study. This low collapse frequency, compared to the 20

kHz resonance frequency of the ultrasonic horn, might explain the difference of pitting rate: high for acoustic cavitation and low for hydrodynamic cavitation.

FIG. 3 shows surface profiles for different cavitation erosion time (4, 16 and 40 min) for hydrodynamic and acoustic cavitation. After 4 min of cavitation, the roughness of the material was not changed drastically from the initial state when the roughness Ra was approximately equal to 60 nm. The difference of roughness between the two types of cavitation may be explained by the difference of bubble sizes. Difference of aggressiveness can be easily noticed between hydrodynamic and acoustic cavitation. For an identical cavitation erosion times, the roughness Ra is more than five times larger for hydrodynamic cavitation than acoustic cavitation.

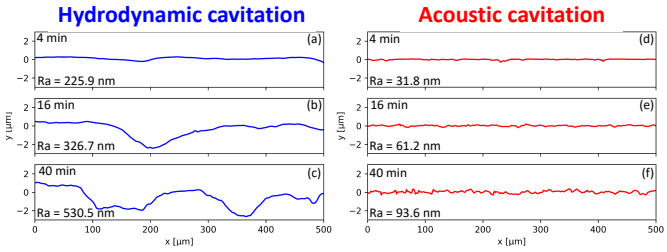

FIG. 3. Surface profiles of X3CrNiMo13-4 QT780 stainless steel exposed to hydrodynamic cavitation (a)-(c) and acoustic cavitation (d)-(f) for different cavitation testing time: (a) and (d) 4 min, (b) and (e) 16 min, (c) and (f) 40 min.

B. Surface evolution

As the cavitation erosion testing time increases, more and more bubbles collapse so that the printed pits cover a bigger and bigger cumulated area. FIG.4 shows the percentage of the surface covered by pits as a function of the cavitation exposure time. The covered surface is defined as the ratio of sum of pits area to total considered area. For hydrodynamic cavitation, the curve tends to a plateau. This could be attributed to the fact that the probability that a bubble collapses in a virgin surface decreases with the cavitation erosion time since the size of the virgin surface diminishes as well. For acoustic cavitation, the covered surface firstly slowly increases until 16 min due to the small sizes of the pits. A rapid growth is then observed, corresponding to the first matter loss. From FIG.4, we observe a shift of the curves between hydrodynamic and acoustic cavitation: the covered surface is more important in the case of hydrodynamic cavitation than acoustic for an identical exposure time. It can be concluded that pits size has more influence than pitting rate on the coverage of the surface. For both types of cavitation, it was observed that bubbles could collapse in the vicinity of existing pits and hence the new pits could partly close the previously created pits. Thus part of solid material might move upward and not solely downward. This could affect the evolution of the covered surface.

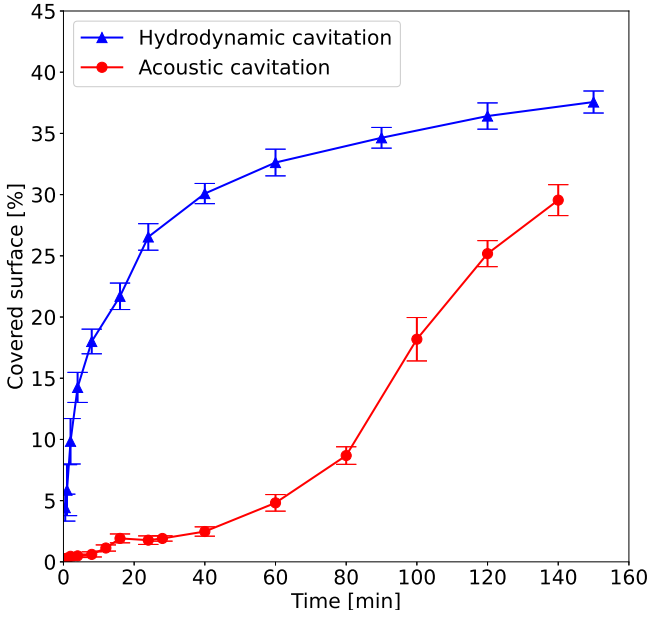

FIG. 4. Percentage of the surface covered by pits as a function of cavitation testing time for X3CrNiMo13-4 QT780 stainless steel. Acoustic cavitation test has been carried out using an ultrasonic horn at 20 kHz on a sample located at 500 μm. Hydrodynamic cavitation test has been carried out in the LEGI cavitation erosion facility at a upstream pressure of 40 bars and at a constant cavitation number of 0.870. Pits have been measured using a 0.2 μm cut-off.

Observation of the surface morphology is not sufficient for understanding the damage mechanism. The material microstructure has to be studied in details.

FIG.5(a) shows a phase map of the X3CrNiMo13-4 QT780 stainless steel with the two phases identified: martensite α' and reversed austenite γ_{rev}. Reversed austenite forms lamellas with a width approximately equal to 150 nm. Presence of these two phases was confirmed using XRD analysis as shown in FIG.5(b). Using integrated peak area from XRD analysis, the volume fraction of reversed austenite has been estimated to 11.9 vol.%. This phase can transform to martensite when a plastic deformation happens: this is known as the transformation-induced plasticity (TRIP) effect. Due to

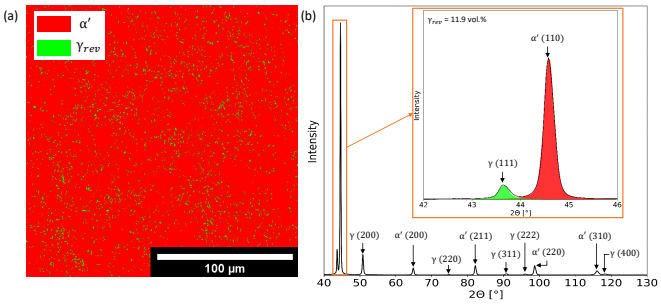

FIG. 5. (a) Phase map from EBSD scan of X3CrNiMo13-4 QT780 before being exposed to cavitation. (b) XRD pattern obtained using Cu-K_α radiation.

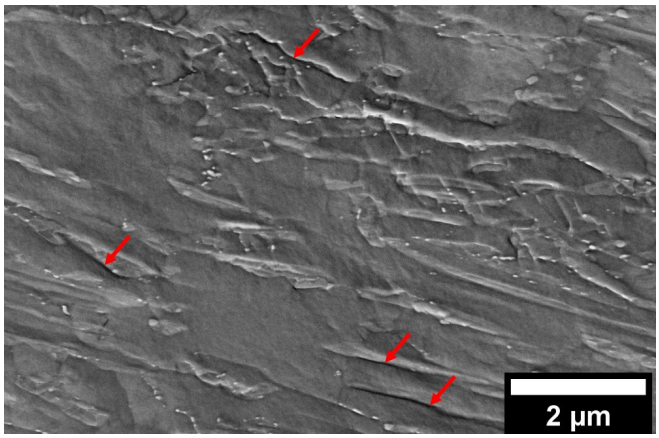

FIG. 6. SEM micrograph of X3CrNiMo13-4 QT780 stainless steel exposed to acoustic cavitation during 15 min. Red arrows show persistent slip bands (PSB) induced by fatigue load.

the change of crystalline structure, this phase transformation causes a volumetric expansion, which produces compressive forces that delay crack initiation and propagation[23,24]. Presence of reversed austenite is thus particularly relevant for the design of materials exposed to cavitation.

At the very beginning of exposition to cavitation, isolated pits appear on the material surface. Pits rapidly overlap and hence totally cover the surface which harden the material. FIG.6 shows the morphology of the eroded surface after being exposed 30 min to acoustic cavitation. First persistent slip bands (PSB) appear at the material surface oriented parallel to the primary activated slip plane. This is the first damage visible after the full coverage of the surface by the pits. PSB is the consequence of mechanical fatigue imposed by the bubble collapses.

SEM micrographs of the same region of X3CrNiMo13-4 QT780 stainless steel sample surface tested for exposure times of 30, 70 and 100 min are shown in FIG.7 for hydrodynamic cavitation (a)-(c) and acoustic cavitation (d)-(f). The effect of the pit size on the material microstructure is different depending on the type of cavitation. Since acoustic cavitation generates small pits as shown in FIG.2, the damage mechanisms induced by this type of cavitation could be more sensitive to the fine microstructure of the material, i.e. typically the martensitic laths. On the other hand, in the case of hydrodynamic cavitation, the observed area in the x3000 SEM observation (FIG.7) is smaller than the average pits diameters for hydrodynamic cavitation. The damage observed on SEM micrographs for hydrodynamic cavitation are hence likely to be located within a pit as also evidenced by the wavelength plotted in FIG.3. As the testing time increases, the deformation state increases as well. Subsequently to the appearance of PSB, cracks initiate at the location of PSB and close to non-metallic elements such as manganese sulfides MnS, carbides $Cr_{23}C_6$ and manganese aluminates Al_2MnO_4 as shown on FIG.7(e).

After this step of initiation, cracks seem to propagate perpendicular to the surface (see yellow circles in FIG.7 (d), (e) and (f)). These sites will be at the origin of the first mass loss. SEM observations suggest that the damage mechanisms with hydrodynamic and acoustic cavitation are identical although the different steps happen for different exposure time. The kinetics of damage mechanisms at the surface is indeed faster for acoustic cavitation due to the high pitting rate. After an exposure time of 100 min, no crack is evidenced at the surface for hydrodynamic cavitation (see FIG.7(c)) while cracks already propagate for acoustic cavitation (FIG.7(f)). Further investigations are required for elucidating damage mechanisms in the volume.

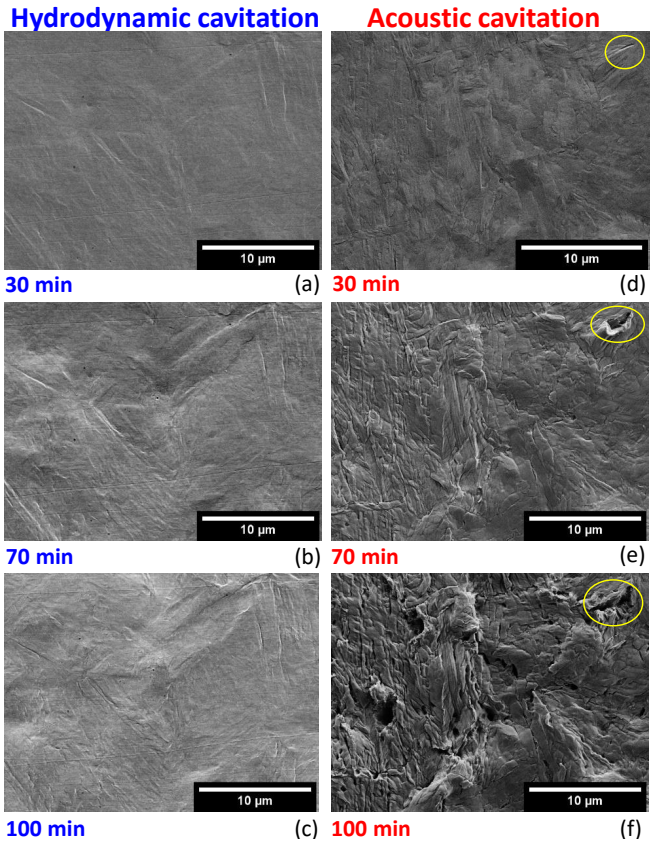

FIG. 7. X3000 SEM micrographs of eroded surfaces by hydrodynamic cavitation (a)-(c) and acoustic cavitation (d)-(f) of X3CrNiMo13-4 QT780 stainless steel for: (a) and (d) 30 min, (b) and (e) 70 min, (c) and (f) 100 min. Yellow circles show example of crack propagating.

IV. CONCLUSION

Mechanical response of martensitic stainless steel X3CrNiMo13-4 QT780 exposed to hydrodynamic and acoustic cavitation were investigated. By analyzing and comparing the material surface, we might draw the following conclusions:

(i) Acoustic cavitation erosion generates small pits at a high frequency on the material while hydrodynamic cavitation erosion produces larger pits at a lower pitting

rate.

(ii) For a given exposure time, the percentage of surface covered by the pits is smaller for acoustic cavitation than for hydrodynamic cavitation. It is concluded that pits' size have more influence than the pitting rate on the surface coverage for the X3CrNiMo13-4 QT780 stainless steel.

(iii) The damage mechanism of X3CrNiMo14-4 QT780 can be decomposed into three main stages. Firstly, persistent slip bands (PSB) appear on the surface. Secondly, cracks initiate and propagate at the PSB locations and non-metallic interfaces and lead to matter removal.

(iv) The steps enumerated at (iii) occur with different kinetics according to the type of cavitation. Surprisingly, despite a small covering rate, acoustic cavitation is faster to initiate cracks than hydrodynamic cavitation.

(v) Cracks initiation and propagation will be further studied in volume using in-situ X-ray tomography. These observations will help the construction of a damage model to be implemented in simulations of cavitation erosion.

ACKNOWLEDGMENTS

This project was funded by the Hydro'like Chair supported by the Grenoble INP Foundation thanks to a donation from General Electric. Maxence Buttard is acknowledged for his help.

[1] J.-P. Franc and J.-M. Michel, en*Fundamentals of Cavitation* (Springer Science & Business Media, 2006) google-Books-ID: QJOQYa_oo24C.

[2] A. Karimi and J. L. Martin, "Cavitation erosion of materials," International Metals Reviews **31**, 1–26 (1986), publisher: Taylor & Francis _eprint: https://doi.org/10.1179/imtr.1986.31.1.1.

[3] L. Rayleigh, "VIII. On the pressure developed in a liquid during the collapse of a spherical cavity," The London, Edinburgh, and Dublin Philosophical Magazine and Journal of Science **34**, 94–98 (1917), publisher: Taylor & Francis _eprint: https://doi.org/10.1080/14786440808635681.

[4] F. Caupin and E. Herbert, en"Cavitation in water: a review," Comptes Rendus Physique Nucleation, **7**, 1000–1017 (2006).

[5] A. N. Allenstein, C. M. Lepienski, A. J. A. Buschinelli, and S. F. Brunatto, en"Improvement of the cavitation erosion resistance for low-temperature plasma nitrided Ca-6NM martensitic stainless steel," Wear **309**, 159–165 (2014).

[6] A. K. Krella, D. E. Zakrzewska, and A. Marchewicz, en"The resistance of S235JR steel to cavitation erosion," Wear **452-453**, 203295 (2020).

[7] G. Gao and Z. Zhang, en"Cavitation erosion mechanism of 2Cr13 stainless steel," Wear **488-489**, 204137 (2022).

[8] R. F. Patella, J.-L. Reboud, and A. Archer, en"Cavitation damage measurement by 3D laser profilometry," Wear **246**, 59–67 (2000).

[9] M. Dular, B. Bachert, B. Stoffel, and B. Širok, en"Relationship between cavitation structures and cavitation damage," Wear **257**, 1176–1184 (2004).

[10] J.-P. Franc, M. Riondet, A. Karimi, and G. L. Chahine, en"Material and velocity effects on cavitation erosion pitting," Wear **274-275**, 248–259 (2012).

[11] A. Abouel-Kasem, A. E. El-Deen, K. M. Emara, and S. M. Ahmed, "Investigation Into Cavitation Erosion Pits," Journal of Tribology **131** (2009), 10.1115/1.3075863.

[12] M. Dular and A. Osterman, en"Pit clustering in cavitation erosion," Wear **265**, 811–820 (2008).

[13] C. Haosheng and L. Shihan, en"Inelastic damages by stress wave on steel surface at the incubation stage of vibration cavitation erosion," Wear **266**, 69–75 (2009).

[14] J.-P. Franc, "Incubation Time and Cavitation Erosion Rate of Work-Hardening Materials," Journal of Fluids Engineering **131** (2009), 10.1115/1.3063646.

[15] M. Gavaises, F. Villa, P. Koukouvinis, M. Marengo, and J.-P. Franc, en"Visualisation and les simulation of cavitation cloud formation and collapse in an axisymmetric geometry," International Journal of Multiphase Flow **68**, 14–26 (2015).

[16] J. C. R. Hunt, C. J. Abell, J. A. Peterka, and H. Woo, en"Kinematical studies of the flows around free or surface-mounted obstacles; applying topology to flow visualization," Journal of Fluid Mechanics **86**, 179–200 (1978), publisher: Cambridge University Press.

[17] M. Tanaka and C. S. Choi, "The Effects of Carbon Contents and M_s Temperatures on the Hardness of Martensitic Fe-Ni-C Alloys," Transactions of the Iron and Steel Institute of Japan **12**, 16–25 (1972).

[18] A. Philipp and W. Lauterborn, en"Cavitation erosion by single laser-produced bubbles," Journal of Fluid Mechanics **361**, 75–116 (1998), publisher: Cambridge University Press.

[19] T. Makuta, R. Suzuki, and T. Nakao, en"Generation of microbubbles from hollow cylindrical ultrasonic horn," Ultrasonics **53**, 196–202 (2013).

[20] J. Lee, M. Ashokkumar, S. Kentish, and F. Grieser, "Determination of the Size Distribution of Sonoluminescence Bubbles in a Pulsed Acoustic Field," Journal of the American Chemical Society **127**, 16810–16811 (2005), publisher: American Chemical Society.

[21] S. C. Roy, *Modeling and analysis of material behavior during cavitation erosion*, PhD Thesis, Université Grenoble Alpes (2015).

[22] M. Ylönen, J.-P. Franc, J. Miettinen, P. Saarenrinne, and M. Fivel, en"Shedding frequency in cavitation erosion evolution tracking," International Journal of Multiphase Flow **118**, 141–149 (2019).

[23] G. B. Olson, en"Transformation Plasticity and Toughening," Le Journal de Physique IV **06**, C1–418 (1996), publisher: EDP Sciences.

[24] J. Chiang, B. Lawrence, J. D. Boyd, and A. K. Pilkey, en"Effect of microstructure on retained austenite stability and work hardening of TRIP steels," Materials Science and Engineering: A **528**, 4516–4521 (2011).